Article

Dislocation Nucleation on Grain Boundaries: Low Angle Twist and Asymmetric Tilt Boundaries

Erman Guleryuz [1] and Sinisa Dj. Mesarovic [2,*]

[1] National Center for Supercomputing Applications, University of Illinois at Urbana-Champaign, Urbana, IL 61801, USA; guleryuz@illinois.edu
[2] School of Mechanical and Materials Engineering, Washington State University, Pullman, WA 99164, USA
* Correspondence: mesarovic@mme.wsu.edu

Abstract: We investigate the mechanisms of incipient plasticity at low angle twist and asymmetric tilt boundaries in *fcc* metals. To observe plasticity of grain boundaries independently of the bulk plasticity, we simulate nanoindentation of bicrystals. On the low angle twist boundaries, the intrinsic grain boundary (GB) dislocation network deforms under load until a dislocation segment compatible with glide on a lattice slip plane is created. The half loops are then emitted into the bulk of the crystal. Asymmetric twist boundaries considered here did not produce bulk dislocations under load. Instead, the boundary with a low excess volume nucleated a mobile GB dislocation and additional GB defects. The GB sliding proceeded by motion of the mobile GB dislocation. The boundary with a high excess volume sheared elastically, while bulk-nucleated dislocations produced plastic relaxation.

Keywords: intrinsic dislocations; partial dislocations; molecular dynamics; nanoindentation

1. Introduction

Grain boundaries (GB) play an important role in the plastic deformation of polycrystalline metals [1]. Therefore, understanding of the GB structure and the dislocation nucleation mechanisms at GBs is critical for the understanding of plasticity of polycrystals.

One parameter characterizing the structural weakness of GBs is the GB excess volume, defined as the difference between the average atomic volume of GB atoms and the average atomic volume in the bulk of the crystal. It can be directly measured, experimentally [2–4], and is correlated with other GB properties, such as energy [5,6] and diffusivity [7,8]. Previous atomistic simulations [9–13] of elemental metals have shown a strong correlation between the GB excess volume and several plastic strain accommodation mechanisms under various mechanical loads at low homologous temperatures. Another convenient characterization of the GB structure is in terms of 2D dislocation arrays. Such description is available for low angle symmetric tilt [14] and twist [15–17] boundaries, as well as boundaries between dissimilar crystals with the same crystalline structure [18]. At present, a general method for characterizing all GBs in a similar manner is not available. While most of the literature is concerned with symmetric tilt boundaries, we limit our study to two types of boundaries: small-angle twist boundaries and asymmetric tilt boundaries.

The low angle twist boundaries are characterized by a 2D network of GB dislocations. The nucleation of a mobile lattice dislocation proceeds by distortion of the existing GB dislocation network and combination of existing GB dislocations. Nucleation of dislocations at twist {100} boundaries in Cu has been observed by Liu et al. [19]. In that geometry, dislocations in the boundary network are compatible with the available lattice slip planes, so that the observed nucleation/emission mechanism is simple. This is apparently the only study of the nucleation mechanism. Recently, Bomarito et al. [20] performed a quantitative investigation of strength (independent of mechanism) of twist GBs in

aluminum, and found that no usual grain boundary descriptors can predict the strength, indicating that significant advances in understanding the nucleation mechanisms are needed. In the present study, we find that a nucleation mechanism deformation and combination of the existing GB dislocations produces lattice dislocations.

Inelastic deformation of asymmetric tilt boundaries is known to occur by several distinct mechanisms: GB sliding by uncorrelated atomic shuffling [10] similar to the intermittent flipping mechanism in granular materials [21], nucleation of lattice dislocations [10,22], GB migration [10,23,24], faceting [23], and motion of a mobile GB dislocation [24]. Here, we find that the nucleation of GB dislocation occurs only for a dense GB (low excess volume) and that it is accompanied by nucleation of lattice partials which create short stacking faults adjacent to the boundary.

To elucidate behavior of grain boundaries with minimal interaction with bulk lattice dislocation structures, we simulate nanoindentation in the vicinity of the grain boundary. Such a loading configuration produces localized high stresses at grain boundaries and only a delayed nucleation in the bulk of the crystal. The methodology of atomistic simulations for nanoindentation problems is well established [25–28].

The paper is organized as follows. In Section 2, we provide details of the computational method. In Sections 3 and 4, we present computational results for low angle twist boundaries, and asymmetric tilt boundaries, respectively. A discussion and summary are given in Section 5.

2. Computational Methods

Molecular dynamics (MD) simulations of spherical indentations in the vicinity of GBs are performed using the open source code LAMMPS [29]. Copper bicrystals containing asymmetric tilt boundaries (ATB) and aluminum bicrystals with low angle twist boundaries (LATB) are modeled with embedded atom method potentials [30,31]. A schematic illustration of the simulation cell for the case of ATBs is shown in Figure 1. Bicrystals with ATBs are constructed by the rotation of the grain B around the $[\bar{1}11]$ axis. The specimen consists of approximately 20 million atoms. Periodic boundary conditions are applied in the x and y directions.
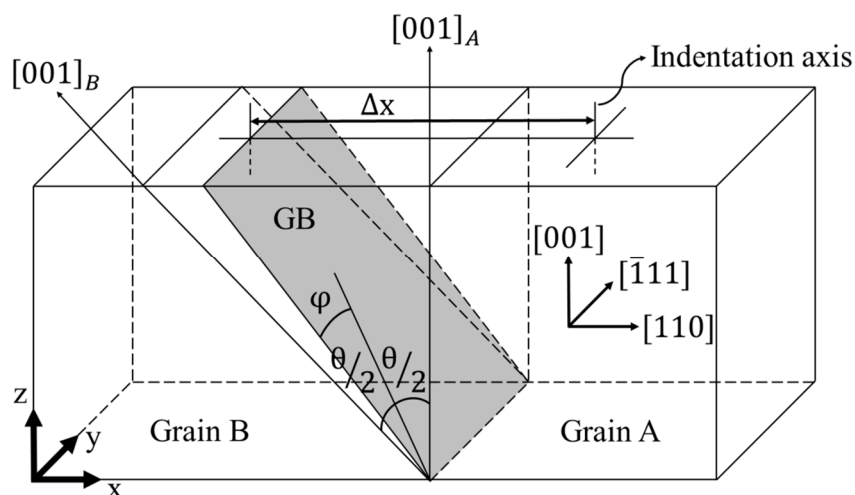

Figure 1. A schematic illustration of the MD simulations of nanoindentation of a *fcc* bicrystal with a $[\bar{1}11]$ asymmetric tilt boundary. Angle φ defines the inclination and equals to the angle between the GB plane and the bisector of the misorientation angle θ. The axis of indentation is located at the center along the y direction and aligned with the normal of the indentation surface. Δx specifies the offset along the x axis between the axis of indentation and the GB on the indentation surface. The specimen has dimensions of 80 nm, 80 nm, and 40 nm in the x, y, and z directions, respectively.

The geometry of the low angle twist boundaries is much simpler. The indentation is still in the [001] direction in grain A; the boundary plane is (111). The twist angle represents the rotation of grain B with respect to grain A around the [111] axis.

The simulations consist of three steps: initial structure generation, thermal equilibration, and displacement controlled indentation. Initial near-equilibrium bicrystal structures were created by energy minimizations using the Polak-Ribiere version of the conjugate gradient method [32].

The relaxed structures were thermally equilibrated for 20 ps at 10 K while all atoms were coupled to a Langevin thermostat [33]. The velocity Verlet time integration algorithm with a time step of 0.002 ps was used. Indentations were performed into thermalized bicrystals at a rate of 0.01 nm/ps. During the indentations, a Langevin thermostat at 10 K was coupled to the atoms within a ten-atomic-layer thick skin region at the lateral and bottom sides of the bicrystal. In addition, five bottom-most layers of atoms in the *z* direction were kept fixed in their lattice positions to anchor the bicrystal. Periodic boundary conditions are applied in the *x* and *y* directions.

The excess volume (given per unit area of the interface *S*) is computed as:

$$V_e = (V - V_o)/S \tag{1}$$

where *V* and V_o are the control volume encompassing the GB and the volume of the perfect crystal containing an equal number of atoms, respectively.

A spherical indenter was modeled with a strong repulsive potential [34]:

$$V_i = kH(R - r_i)(R - r_i)^3 \tag{2}$$

where r_i, k, $H(*)$, and R are the distance from the atom i to the center of the indenter, the force constant, the Heaviside step function, and the indenter radius, respectively. By trial and error, we determined that for $R = 10$ nm and the interatomic potentials used here, the value $k = 480 \, \mathrm{nN/nm}^2$ (close to the 530 nN/nm^2 used in [34]) is sufficiently high to emulate the rigid surface.

Structure and defect visualizations were carried out with OVITO [35], an open-source post-processing software for atomistic datasets. Defect characterizations were performed based on the centrosymmetry parameter (CSP) [33]. Local deviations from centrosymmetry in certain lattice types, such as *fcc* and *bcc*, can be used to identify crystalline defects. CSP is defined, to quantify such deviations, as follows:

$$CSP = \sum_{i=1}^{N/2} \left| \boldsymbol{R}_i + \boldsymbol{R}_{i+N/2} \right|^2 \tag{3}$$

where N is the number of nearest neighbors of a central atom (12 in *fcc* crystals). $\boldsymbol{R}_i$ and $\boldsymbol{R}_{i+N/2}$ are position vectors from the central atom to the pairs of nearest neighbors. There are $N(N-1)/2$ possible nearest neighbor pairs that can contribute to the sum in the CSP formula. The quantity $\left| \boldsymbol{R}_i + \boldsymbol{R}_{i+N/2} \right|^2$ is calculated for all possible nearest neighbor pairs and only the $N/2$ smallest values are used to compute the CSP. These $N/2$ smallest values typically correspond to pairs of atoms in symmetrically opposite positions (in which case the sum of position vectors for the pair will be zero) around the central atom. Accordingly, the CSP value will be zero (or near zero in the case of thermal perturbations) for lattice points in a centrosymmetric crystal. Similarly, the local centrosymmetry will be maintained after homogeneous elastic deformations. In the existence of a crystal defect, however, the symmetry is broken and CSP will be a larger positive value. The practical value of CSP comes from its ability to distinguish lattice defects from regions that underwent large homogeneous elastic deformations as well as from its ability to separate different defect types (e.g., dislocation cores, stacking faults, GBs).

3. Low-Angle Twist Boundaries

The relaxed structures of twist boundaries have been described by Dai et al. [16,17]. We have observed similar networks in our simulations of Al bicrystals, as shown in Figure 2. The boundaries

contain periodic structures of dislocations such that the net effect of the Burgers vectors in a period is the nominal twist angle for the boundary. We note that the networks are similar for all twist angles analyzed here, but the period is shortened with the increasing twist angle. The same Burgers vector repeated in the smaller period accomplishes larger twist.
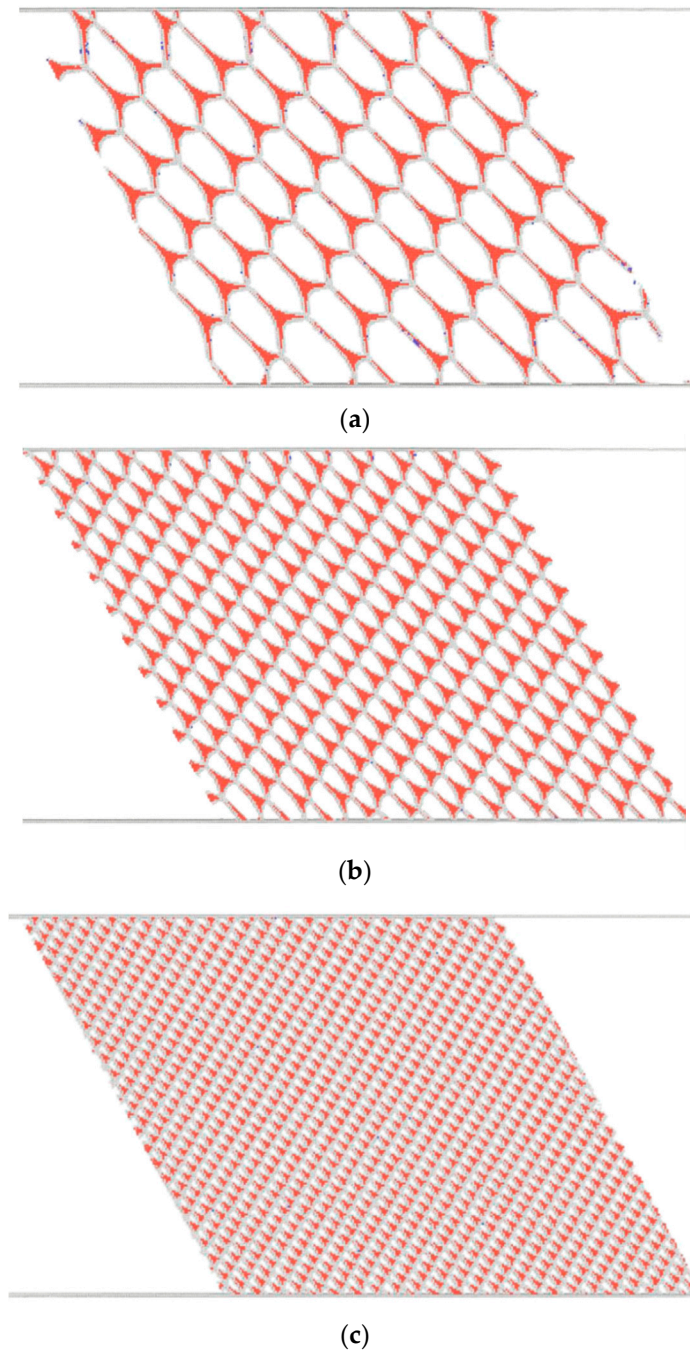

(a)

(b)

(c)

Figure 2. Intrinsic dislocation structure at low angle twist boundaries in Al. The coloring is based on the centrosymmetry (CSM) parameter [33]. Gray lines are dislocation lines, red areas represent stacking faults. (**a**) 2° twist; (**b**) 4° twist; and (**c**) 6° twist.

Another quantitative change with increasing twist angle bears emphasis, as it gradually produces a qualitative change. In the 2° twist boundary, the stacking faults are much smaller than the regular (*fcc*) stacking regions, so that the resulting network can be loosely described as a coarse hexagonal

network with nearly full dislocations. As the twist angle increases, the stacking fault area becomes nearly equal to the regular stacking area, so that the closest description of the network is a dense triangular network of partials.

Load-displacement curves are shown in Figure 3. The first load drops represent dislocation nucleation events at the grain boundary. Two effects of the twist angle are observable: (1) a denser dislocation network, associated with a larger twist angle, implies a more difficult nucleation; and (2) the 4° and 6° boundaries appear to be slightly more elastically compliant prior to dislocation nucleation. These observations can be explained once the nucleation mechanism is understood.
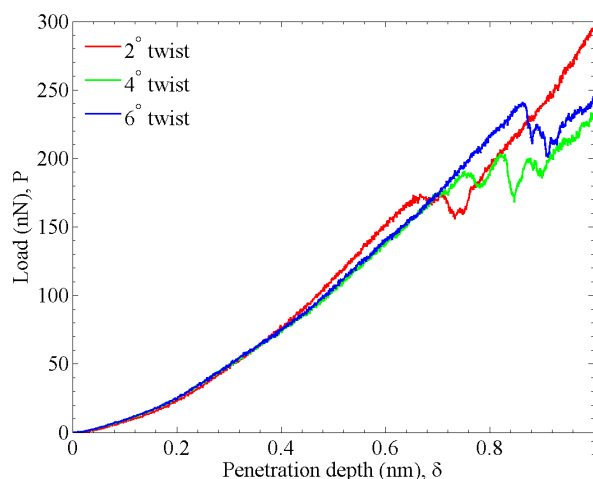

Figure 3. Load-displacement curves for the nanoindentation near the low angle twist boundaries in Al.

Dislocation nucleation proceeds in two steps, as shown in Figure 4 for the 4° twist boundary. First, the existing network of intrinsic GB dislocations deforms (Figure 4 left). Although this stage of deformation includes motion of GB dislocations, the process is mechanically reversible. Thus, the pseudo-elastic deformation prior to nucleation is, in fact, partially dissipative. The next step (Figure 4 right) is described in detail in Figure 5. Splitting of a network node results in the creation of a dislocation segment with a <011> Burgers vector, which glides in the lattice slip plane.
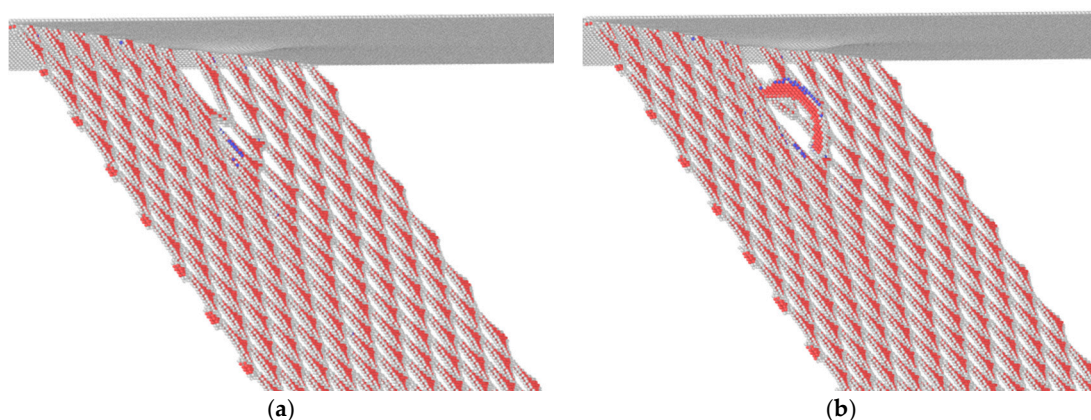

(**a**)   (**b**)

Figure 4. Dislocation nucleation mechanisms at the 4° twist boundary. The gray at the top is the indentation surface. (**a**) The network of intrinsic GB dislocations deforms first; and (**b**) the dislocation lines in the network combine to form the bulk crystal dislocation half loop, which then expands into the crystal. The details of the nucleation mechanism are shown in Figure 5.
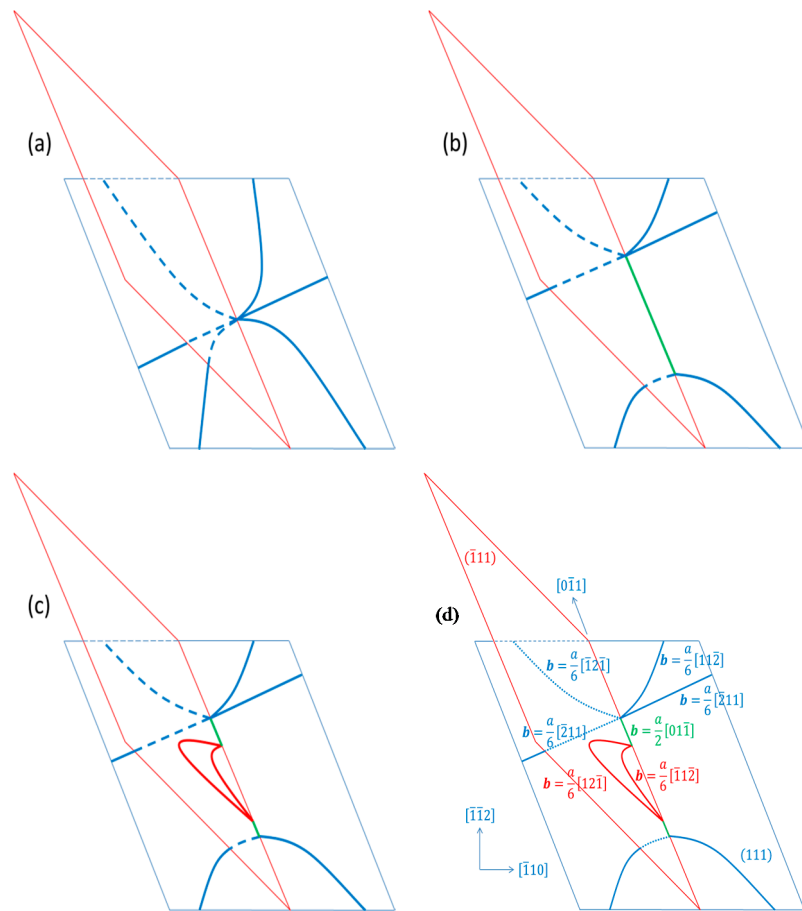
Figure 5. Geometry of dislocation nucleation at a low angle twist boundary. (**a**) Initial geometry at the intersection node of intrinsic GB dislocation. The lattice slip plane shown in red; (**b**) under the load, the network deforms, the node splits, and new dislocation is created (green) which can glide in the lattice slip plane; (**c**) two half loops of partials, separated by the stacking fault expand into the crystal; and (**d**) quantitative details of the geometry: Burgers vectors, planes, and directions.

The observations made in connection to the load-displacement curve (Figure 3) can now be explained. A long segment of nearly-full dislocation in the coarse hexagonal network (Figure 2a) is easily deformed without much distortion in the surrounding network. Such motion is limited to a single segment and is not observable in the macroscopic force-displacement curve. Finally, the narrow stacking fault is easily pinched, so that the full lattice dislocation emerges relatively easily without observable prior pseudo-elastic deformation. In contrast, the short segments of dense triangular networks (Figure 2b,c) are difficult to move without distortion of the large portion of the network, which is observable macroscopically as pseudo-elastic deformation. Pinching of the stacking between two short partials is also difficult, resulting in a high nucleation load.

4. Asymmetric Tilt Boundaries

Bicrystals are constructed by the rotation of grain B around the $[\bar{1}11]$ tilt axis. We consider two asymmetric tilt boundaries (ATBs): the dense GB (with small excess volume) and the loose GB (with large excess volume). Details of the ATB geometry are given in Table 1. The atomic structures of the GBs after energy minimizations and the misalignment of slip systems across neighboring grains are shown in Figure 6.
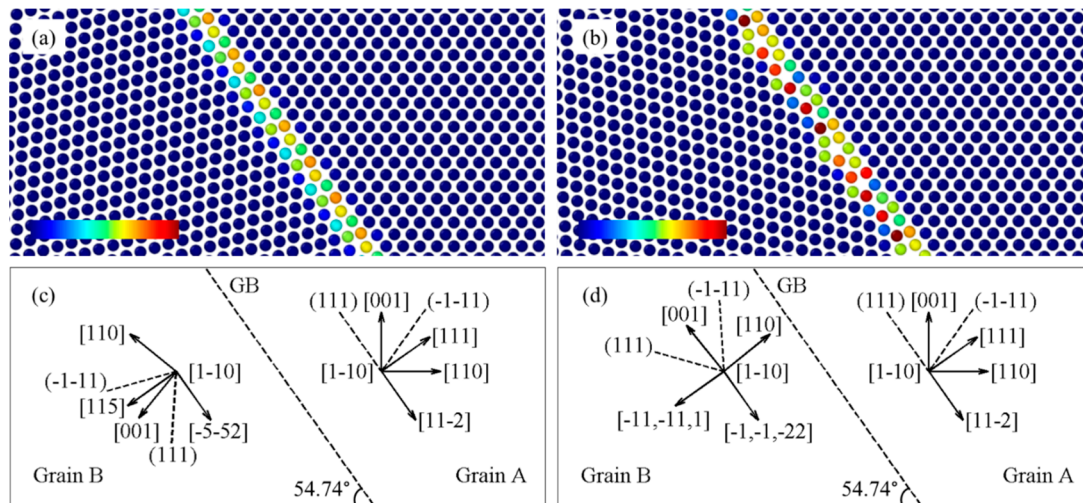
Figure 6. Relaxed GB structures and misalignments of the slip systems across neighboring grains. (**a**,**c**): Cu bicrystal with the dense boundary; (**b**,**d**): Cu bicrystal with the loose boundary. Atomic snapshots are taken along the $[1\bar{1}1]$ tilt axis (points out of the paper). Atoms are colored according to the centrosymmetry parameter. The blue end of the color bar corresponds to zero, while the red end of the color bar corresponds to ten.

Table 1. Geometric parameters of the asymmetric tilt boundaries.

	Tilt Axis	Misorientation Angle (θ)	Inclination Angle (ϕ)	GB Planes	Excess Volume (nm)
Dense GB	$[\bar{1}10]$	141.06° (Σ9)	35.26°	$(111)_A$; $(115)_B$	0.01534
Loose GB	$[\bar{1}10]$	38.94° (Σ9)	15.79°	$(111)_A$; $(11\,11\,\bar{1})_B$	0.02679

The force-displacement curves for nanoindentations in the vicinity of the dense and loose GB are shown in Figure 7. For both tilt GBs, two offset values (Δx) representing the normal distance between the center of indentation and the intersection of the grain boundary with the free surface are considered: 0.5R and R, where R = 10 nm is the radius of the indenter. Nanoindentation into a single crystal is performed as a benchmark.
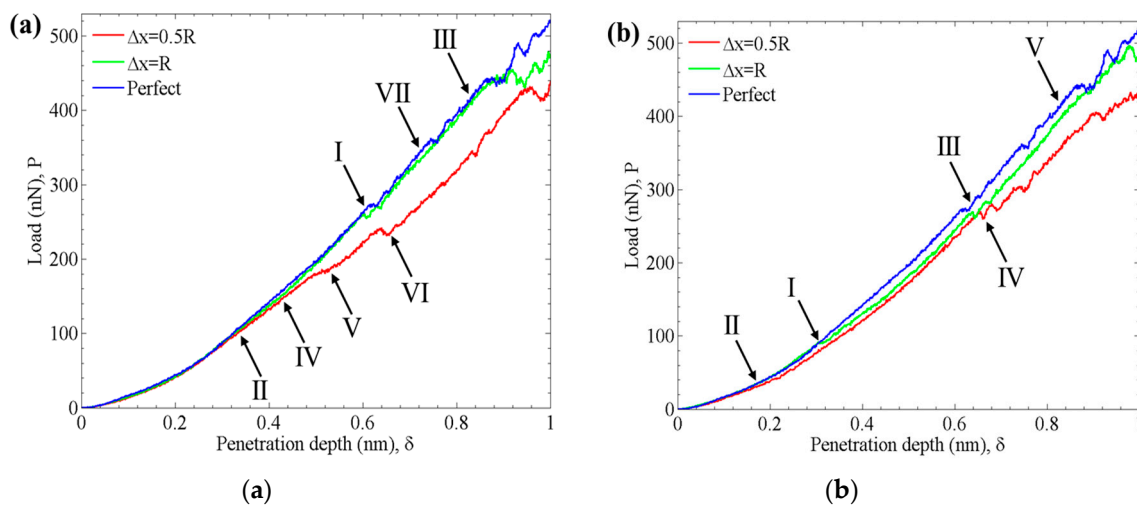

Figure 7. Indentation load as a function of penetration depth for spherical indentation into Cu bicrystals and a Cu single crystal. (**a**) Bicrystal with the dense boundary; and (**b**) bicrystal with the loose boundary. The arrows and Roman numerals are explained in the text.

Previous atomistic simulations [34,36–39] of indentations into single crystals link discontinuities (load drops) on the *P-δ* curve to the nucleation of dislocations. In the case of indentation near a GB, the sequence of events is more complex (Figure 7).

For the dense GB and Δx = R, the *P-δ* curve closely follows the elastic single crystal curve until the first load drop (point I in Figure 7a). For Δx = 0.5R, an early deviation from the nominal curve is observed (point II in Figure 7a). This indicates the activation of different inelastic deformation mechanisms depending on the indentation proximity to the GB.

For the loose GB, the early deviation from the elastic single crystal curve is observed for both offset values (points I and II in Figure 7b), indicating the same deformation mechanism. For both offset values, the deviation from the elastic single crystal curve occurs at smaller loads compared to the respective cases with the dense GB, but the indentation closer to the boundary produces the deviation at a lower load, consistent with previous observations [26].

For the dense GB, the sequence of inelastic deformation mechanisms is as follows when Δx = 0.5R (Figure 7a):

- Point IV: nucleation of Shockley partials from the GB;
- Point V: nucleation of a boundary dislocation loop; and
- Point VI: dislocation nucleation in the bulk, under the indenter.

The sequence of inelastic deformation mechanisms is different when Δx = R:

- Point I: dislocation nucleation in the bulk, under the indenter;
- Point VII: nucleation of Shockley partials from the GB; and
- Point III: nucleation of a boundary dislocation loop.

Notably, for the dense GB and the offset Δx = R, plasticity is observable in the load-displacement curve after the dislocation nucleation in the bulk (point I in Figure 7a). This is in contrast to the case with Δx = 0.5R, where the GB sliding precedes the dislocation activity in the bulk of the crystal. In both simulations, the bulk nucleated dislocations do not reach the grain boundary and interact with it only through the stress field.

A 3D snapshot of the microstructure near the dense GB at *δ* = 0.85 nm and, when Δx = R (point III in Figure 7a) is shown in Figure 8a. The glide of a GB dislocation loop and the development of a plastic zone beneath the indenter are visible. The nucleation and propagation of the GB dislocation loop lead to the sliding of the boundary. The cross-sectional view of the 3D snapshot along the $[\bar{1}11]$ tilt axis is shown in Figure 8b. The region marked with the dashed square is magnified (Figure 8c) for a detailed look into the dislocation activity. The GB dislocation loop glides on the (111) plane parallel to the interface and has a Burgers vector (expressed with the lattice directions in the grain A) of $\boldsymbol{b_1} = 2a/7\left[11\bar{2}\right]$ (111), where *a* is the lattice parameter. Emergence of two Shockley partial dislocation loops into grain B is observed as a local relaxation mechanism. Shockley partials have Burgers vectors (expressed with the lattice directions in grain B) of $\boldsymbol{b_2} = \boldsymbol{b_3} = a/6\,[112]\,(\bar{1}\bar{1}1)$ and are separated by three {111} interplanar distances.

In the case of the loose GB, elastic stretching of GB atoms leads to early deviation from the single crystal curve (points I and II in Figure 7b) with both offset (Δ*x*) values. This is followed by sequential nucleation of dislocation loops in the bulk of the crystal (points III and IV in Figure 7b).

A 3D snapshot of the microstructure near the loose GB at *δ* = 0.85 nm and, when Δ*x* = R (point V in Figure 7b), is shown in Figure 9a. A cross-sectional view of the 3D snapshot along the $[\bar{1}11]$ tilt axis is shown in Figure 9b. The area marked by the dashed square is magnified in Figure 9c to inspect the structural transformations. The displacement vector field computed between the initial configuration and the instant at *δ* = 0.85 nm is superposed to the magnified view. A homogeneous displacement field in grain A and a structural transformation in the GB are visible. The GB shears by elastic bond stretching and rotation. The plasticity is confined to the bulk nucleated dislocations.
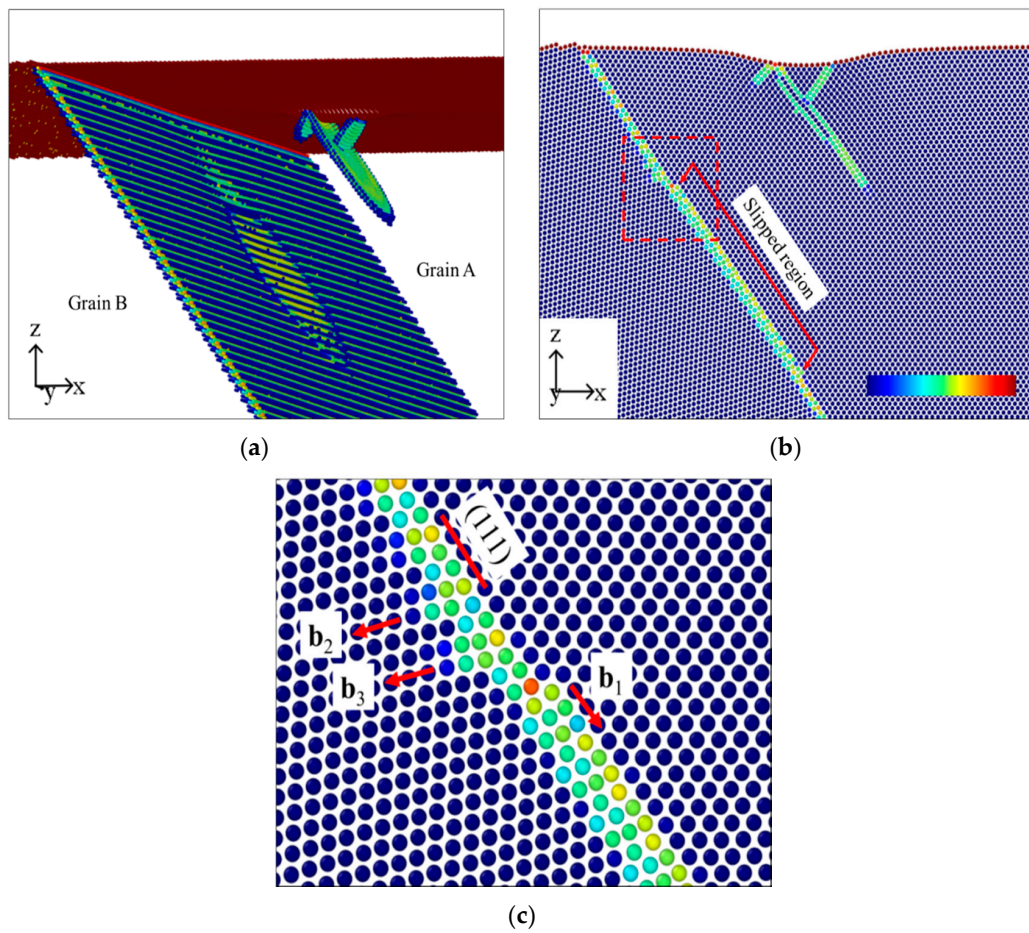
Figure 8. Atomic configuration during the indentation near ($\Delta x = R$) the dense GB at $\delta = 0.85$ nm. Atoms are colored according to CSP; x, y and z axes of the simulation cell are aligned with lattice directions $[110]_A$, $[\overline{1}10]_A$, and $[001]_A$. (**a**) 3D view. *fcc* atoms are removed for the clarity of illustration; (**b**) cross-sectional view. Atoms on two adjacent $(2\overline{2}0)$ planes at the center of the bicrystal are shown along the along $[1\overline{1}0]$ tilt axis; and (**c**) the magnified view of the region marked with the dashed square in (**b**).
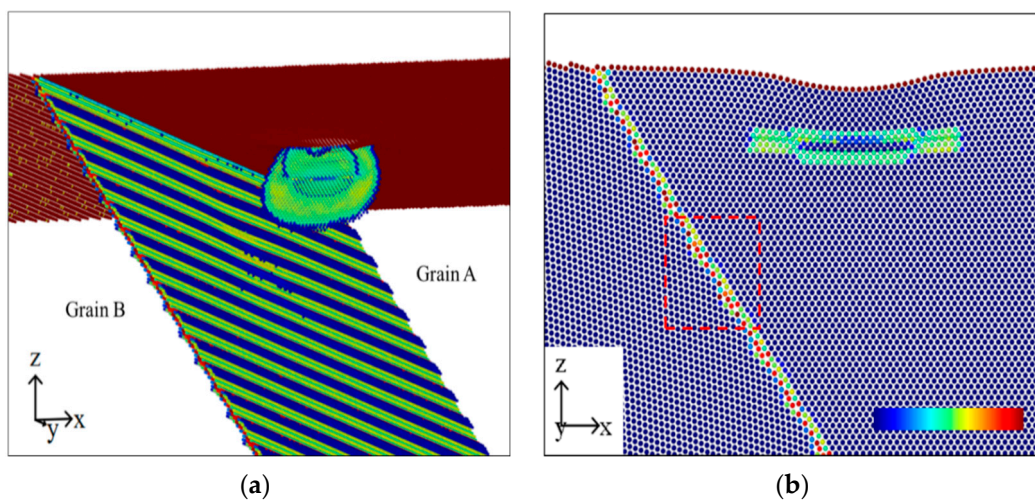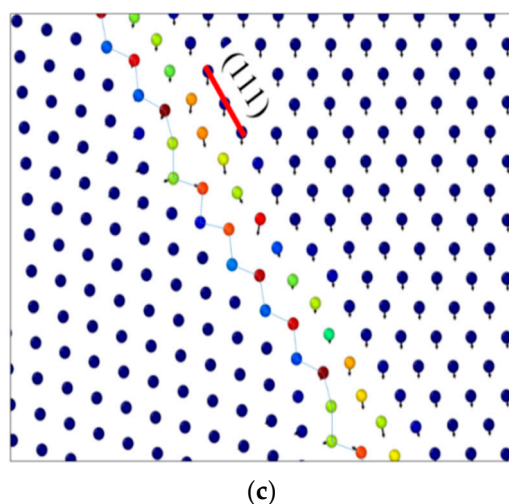

Figure 9. *Cont.*

(**c**)

Figure 9. Atomic configuration during the indentation near ($\Delta x = R$) the loose GB at $\delta = 0.85$ nm. Atoms are colored according to CSP; x, y, and z axes of the simulation cell are respectively aligned with lattice directions $[110]_A$, $[\bar{1}10]_A$, and $[001]_A$. (**a**) 3D view. *fcc* atoms are removed for the clarity of illustration; (**b**) cross-sectional view. Atoms on two adjacent $(2\bar{2}0)$ planes at the center of the bicrystal are shown along the $[1\bar{1}0]$ tilt axis; and (**c**) the magnified view of the region marked with the dashed square in (**b**).

5. Summary and Discussion

Low angle twist boundaries can be a source of lattice dislocations. Lattice dislocations are generated from intrinsic GB dislocation network. Initially, the boundary dislocation network deforms until a dislocation segment which can glide on the lattice plane is produced. The nucleation stress increases with the network density, but denser networks exhibit pseudo-elastic deformation prior to nucleation of a lattice dislocation. To our knowledge, the nucleation mechanism involving the deformation of the GB dislocation network and combination of existing dislocations has not been observed previously, although the fact of nucleation has been observed [19,20]. As the twist angle changes, so does the geometry of the GB dislocation network [15,17]. The immediate question is whether such, or similar, mechanisms operate at all twist angles. While a distortion of the network producing a lattice compatible dislocation segment is always theoretically possible, the nucleation stresses and the detailed mechanism will vary with the geometry of the network. Investigation and quantification of nucleation mechanisms for the variety of twist boundary networks [15,17] is one area of future research.

In our study of asymmetric tilt boundaries, nucleation of lattice dislocations at the boundary was not observed. Bulk nucleation occurs first, and dislocations nucleated in the bulk may then react with grain boundaries. Our choice of nanoindentation allowed us to focus on GB dislocations and avoid their interactions with bulk nucleated dislocations. Loose GBs (high excess volume) exhibit a significant elastic shear at the GB; plastic relaxation occurs by bulk dislocation nucleation. Dense GBs (low excess volume) favor nucleation of well-defined mobile GB dislocation loops whose expansion produces GB sliding. Nucleation of such dislocation requires nucleation of additional defects at the GB, as observed previously [24]. Plasticity of asymmetric tilt boundaries is clearly a complex problem featuring multiple competing deformation mechanisms [10,22–24]. The unifying mathematical description of such boundaries is still an open problem.

Finally, the continuum models which take into account the size effect arising from grain boundaries have been mostly focused on boundaries as obstacles for dislocation motion [40–42]. The role of grain boundaries as sources of dislocations has not been modeled on the continuum level.

References

1. Armstrong, R.W.; Elban, W.L.; Walley, S.M. Elastic, Plastic, Cracking Aspects of the Hardness of Materials. *Int. J. Mod. Phys. B* **2013**, *27*, 1330004. [CrossRef]

2. Steyskal, E.; Oberdorfer, B.; Sprengel, W.; Zehetbauer, M.; Pippan, R.; Würschum, R. Direct experimental determination of grain boundary excess volume in metals. *Phys. Rev. Lett.* **2012**, *108*, 055504. [CrossRef] [PubMed]

3. Shen, T.D.; Zhang, J.; Zhao, Y. What is the theoretical density of a nanocrystalline material? *Acta Mater.* **2008**, *56*, 3663–3671. [CrossRef]

4. Shvindlerman, L.S.; Gottstein, G.; Ivanov, V.A.; Molodov, D.A.; Kolesnikov, D.; Łojkowski, W. Grain boundary excess free volume-direct thermodynamic measurement. *J. Mater. Sci.* **2006**, *41*, 7725–7729. [CrossRef]

5. Olmsted, D.L.; Foiles, S.M.; Holm, E.A. Survey of computed grain boundary properties in face-centered cubic metals: I. Grain boundary energy. *Acta Mater.* **2009**, *57*, 3694–3703. [CrossRef]

6. Wolf, D. Structure-energy correlation for grain boundaries in F.C.C. metals-I. Boundaries on the (111) and (100) planes. *Acta Metall.* **1989**, *37*, 1983–1993. [CrossRef]

7. Chuvil'deev, V.N. Micromechanism of deformation-stimulated grain-boundary self-diffusion: I. Effect of excess free volume on the free energy and diffusion parameters of grain boundaries. *Phys. Met. Metallogr.* **1996**, *81*, 463–468.

8. Aaron, H.B.; Bolling, G.F. Free volume as a guide to grain boundary phenomena. *Scr. Mater.* **1972**, *6*, 553–562. [CrossRef]

9. Van Swygenhoven, H.; Derlet, P.M. Grain-boundary sliding in nanocrystalline fcc metals. *Phys. Rev. B* **2001**, *64*, 224105. [CrossRef]

10. Sansoz, F.; Molinari, J.F. Mechanical behavior of Σ tilt grain boundaries in nanoscale Cu and Al: A quasicontinuum study. *Acta Mater.* **2005**, *53*, 1931–1944. [CrossRef]

11. Spearot, D.E.; Tschopp, M.A.; Jacob, K.I.; McDowell, D.L. Tensile strength of <100> and <110> tilt bicrystal copper interfaces. *Acta Mater.* **2007**, *55*, 705–714. [CrossRef]

12. Tucker, G.J.; Tschopp, M.A.; McDowell, D.L. Evolution of structure and free volume in symmetric tilt grain boundaries during dislocation nucleation. *Acta Mater.* **2010**, *58*, 6464–6473. [CrossRef]

13. Burbery, N.J.; Das, R.; Ferguson, W.G. Modelling with variable atomic structure: Dislocation nucleation from symmetric tilt grain boundaries in aluminium. *Comput. Mater. Sci.* **2015**, *101*, 16–28. [CrossRef]

14. Sutton, A.P.; Balluffi, R.W. *Interfaces in Crystalline Materials*; Oxford University Press: Oxford, UK, 1995.

15. Schwartz, D.; Bristowe, P.D.; Vitek, V. Dislocation structure and energy of high angle {001} twist boundaries: A computer simulation study. *Acta Metall.* **1988**, *36*, 675–687. [CrossRef]

16. Dai, S.; Xiang, Y.; Srolovitz, D.J. Structure and energy of (111) low-angle twist boundaries in Al, Cu and Ni. *Acta Mater.* **2013**, *69*, 162–174. [CrossRef]

17. Dai, S.; Xiang, Y.; Srolovitz, D.J. Atomistic, generalized Peierls-Nabarro and analytical models for (111) twist boundaries in Al, Cu and Ni for all twist angles. *Acta Mater.* **2014**, *61*, 1327–1337. [CrossRef]

18. Beyerlein, I.J.; Wang, J.; Zhang, R. Mapping dislocation nucleation behavior from bimetal interfaces. *Acta Mater.* **2013**, *61*, 7488–7499. [CrossRef]

19. Liu, X.M.; You, Z.C.; Liu, Z.L.; Nie, J.F.; Zhuang, Z. Atomistic simulations of tension properties for bi-crystal copper with twist grain boundary. *J. Phys. D Appl. Phys.* **2009**, *42*, 035404. [CrossRef]

20. Bomarito, G.F.; Lin, Y.; Warner, D.H. An atomistic modeling survey of the shear strength of twist grain boundaries in aluminum. *Scr. Mater.* **2015**, *101*, 72–75. [CrossRef]

21. Mesarovic, S.D.J.; Padbidri, J.M.; Muhunthan, B. Micromechanics of dilatancy and critical state in granular matter. *Geotech. Lett.* **2012**, *2*, 61–66. [CrossRef]

22. Tschopp, M.A.; McDowell, D.L. Dislocation nucleation in Σ3 asymmetric tilt grain boundaries. *Int. J. Plast.* **2008**, *24*, 191–217. [CrossRef]

23. Wan, L.; Li, J. Shear responses of $[\bar{1}10]$-tilt {1 1 5}/{1 1 1} asymmetric tilt grain boundaries in fcc metals by atomistic simulations. *Model. Simul. Mater. Sci. Eng.* **2013**, *21*, 055013. [CrossRef]

24. Zhang, L.; Lu, C.; Kiet, T.; Zhao, X.; Pei, L. The shear response of copper bicrystals with Σ11 symmetric and asymmetric tilt grain boundaries by molecular dynamics simulation. *Nanoscale* **2015**, *7*, 7224–7233. [CrossRef] [PubMed]
25. Feichtinger, D.; Derlet, P.M.; Van Swygenhoven, H. Atomistic simulations of spherical indentations in nanocrystalline gold. *Phys. Rev. B* **2003**, *67*, 024113. [CrossRef]
26. Lilleodden, E.T.; Zimmerman, J.A.; Foiles, S.M.; Nix, W.D. Atomistic simulations of elastic deformation and dislocation nucleation during nanoindentation. *J. Mech. Phys. Solids* **2003**, *51*, 901–920. [CrossRef]
27. Nair, A.K.; Parker, E.; Gaudreau, P.; Farkas, D.; Kriz, R.D. Size effects in indentation response of thin films at the nanoscale: A molecular dynamics study. *Int. J. Plast.* **2008**, *24*, 2016–2031. [CrossRef]
28. Sansoz, F.; Stevenson, K.D. Relationship between hardness and dislocation processes in a nanocrystalline metal at the atomic scale. *Phys. Rev. B* **2011**, *83*, 224101. [CrossRef]
29. Plimpton, S. Fast parallel algorithms for short-range molecular dynamics. *J. Comp. Phys.* **1995**, *117*, 1–19. [CrossRef]
30. Mishin, Y.; Mehl, M.J.; Papaconstantopoulos, D.A.; Voter, A.F.; Kress, J.D. Structural stability and lattice defects in copper: Ab initio, tight-binding, and embedded-atom calculations. *Phys. Rev. B* **2001**, *63*, 224106. [CrossRef]
31. Mishin, Y.; Fracas, D.; Mehl, M.J.; Papaconstantopoulos, D.A. Interatomic potentials for monoatomic metals from experimental data and ab initio calculations. *Phys. Rev. B* **1999**, *59*, 3393–3407. [CrossRef]
32. Polak, E.; Ribiere, G. Note sur la convergence de méthodes de directions conjuguées. *Modél. Math. Anal. Numér.* **1969**, *3*, 35–43.
33. Schneider, T.; Stoll, E. Molecular-dynamics study of a three-dimensional one-component model for distortive phase transitions. *Phys. Rev. B* **1978**, *17*, 1302. [CrossRef]
34. Kelchner, C.L.; Plimpton, S.J.; Hamilton, J.C. Dislocation nucleation and defect structure during surface indentation. *Phys. Rev. B* **1998**, *58*, 11085. [CrossRef]
35. Stukowski, A. Visualization and analysis of atomistic simulation data with OVITO-the Open Visualization Tool. *Model. Simul. Mater. Sci. Eng.* **2010**, *18*, 015012. [CrossRef]
36. Van Vliet, K.J.; Li, J.; Zhu, T.; Yip, S.; Suresh, S. Quantifying the early stages of plasticity through nanoscale experiments and simulations. *Phys. Rev. B* **2003**, *67*, 104105. [CrossRef]
37. Zhu, T.; Li, J.; Van Vliet, K.J.; Ogata, S.; Yip, S.; Suresh, S. Predictive modeling of nanoindentation-induced homogeneous dislocation nucleation in copper. *J. Mech. Phys. Solids* **2004**, *52*, 691–724. [CrossRef]
38. Lee, Y.; Park, J.Y.; Kim, S.Y.; Jun, S.; Im, S. Atomistic simulations of incipient plasticity under Al(111) nanoindentation. *Mech. Mater.* **2005**, *37*, 1035–1048. [CrossRef]
39. Miller, R.E.; Rodney, D. On the nonlocal nature of dislocation nucleation during nanoindentation. *J. Mech. Phys. Solids* **2008**, *56*, 1203–1223. [CrossRef]
40. Mesarovic, S.Dj. Plasticity of crystals and interfaces: From discrete dislocations to size-dependent continuum theory. *Theor. Appl. Mech.* **2010**, *37*, 289–332. [CrossRef]
41. Voyiadjis, G.Z.; Faghihi, D.; Zhang, Y. A theory for grain boundaries with strain-gradient plasticity. *Int. J. Solids Struct.* **2014**, *51*, 1872–1889. [CrossRef]
42. Mesarovic, S.D.J.; Forest, S.; Jaric, J.P. Size-dependent energy in crystal plasticity and continuum dislocation models. *Proc. R. Soc. A* **2015**, *471*, 20140868. [CrossRef] [PubMed]